

## RESEARCH: SHORT COMMUNICATION

## Influence of defect type on hydrogen passivation efficacy in multicrystalline silicon solar cells

M.I. Bertoni<sup>1</sup>, S. Hudelson<sup>1</sup>, B.K. Newman<sup>1</sup>, D.P. Fenning<sup>1</sup>, H.F.W. Dekkers<sup>2</sup>, E. Cornagliotti<sup>2</sup>, A. Zuschlag<sup>3</sup>, G. Micard<sup>3</sup>, G. Hahn<sup>3</sup>, G. Coletti<sup>4</sup>, B. Lai<sup>5</sup> and T. Buonassisi<sup>1\*</sup>

<sup>1</sup> Massachusetts Institute of Technology, Cambridge, MA 02139, USA

<sup>2</sup> imec vzw. Kapeldreef 75, 3001 Leuven, Belgium

<sup>3</sup> Department of Physics, University of Konstanz, 78457 Konstanz, Germany

<sup>4</sup> ECN Solar Energy, Westerduinweg 3, NL-1755 LE Petten, The Netherlands

<sup>5</sup> Advanced Photon Source, Argonne National Laboratory, Argonne, IL 60439, USA

### ABSTRACT

We examine the effectiveness of hydrogen passivation as a function of defect type and microstructure at grain boundaries (GBs) in multicrystalline silicon. We analyze a solar cell with alternating mm-wide bare and SiN<sub>x</sub>-coated stripes using laser-beam-induced current, electron backscatter diffraction, X-ray fluorescence microscopy, and defect etching to correlate pre- and post-hydrogenation recombination activity with GB character, density of iron-silicide nanoprecipitates, and dislocations. A strong correlation was found between GB recombination activity and the nature/density of etch pits along the boundaries, while iron silicide precipitates above detection limits were found to play a less significant role. Copyright © 2010 John Wiley & Sons, Ltd.

### KEYWORDS

hydrogen passivation; defects; dislocations; iron; multicrystalline silicon

### \*Correspondence

T. Buonassisi, Massachusetts Institute of Technology, Cambridge, MA 02139, USA.

E-mail: buonassisi@mit.edu

Received 11 February 2010; Revised 20 April 2010

In crystalline silicon solar cells, the introduction of hydrogen is well known to passivate defects and improve the conversion efficiency [1–3]. It has been found that the effectiveness of hydrogen passivation of grain boundaries (GBs) depends on GB character and metal contamination [4–8]. However, a deeper microstructural understanding concerning which defects are most effectively passivated, and which respond poorly to hydrogenation, is needed to guide the optimization of solar cell manufacturing. Those defects with the weakest response to hydrogenation can be most effectively dealt with during other steps in solar cell manufacturing such as crystallization or optimized emitter diffusion.

To investigate the passivation ability of hydrogen on defects at GBs in silicon, a 12.5 × 12.5 mm<sup>2</sup> multicrystalline silicon (mc-Si) solar cell was produced by IMEC. The sample contains both control (bare) and experimental (SiN<sub>x</sub>-coated) regions, to ensure identical thermal profiles for the control and experimental regions during crystal growth and cell processing. After emitter diffusion (845°C, 12 min POCl<sub>3</sub> followed by 18 min drive-in) the sample was selectively masked with a ceramic paste via screen-printing

to create alternating mm-wide stripes of bare and coated regions during the deposition of the SiN<sub>x</sub> antireflection coating and resulting hydrogenation (PECVD, 400°C, 6 min). The ceramic paste was removed after SiN<sub>x</sub> deposition using an H<sub>2</sub>SO<sub>4</sub>:H<sub>2</sub>O<sub>2</sub> cleaning solution. Finally, silver- and aluminum-based metal contacts were screen-printed on the front and back, respectively, and fired (RTA, T<sub>max</sub> = 800°C, 4 min) in a conventional belt furnace. The electrical performance of the solar cell was characterized using laser-beam-induced current (SR-LBIC) [9] at the University of Konstanz at 833 and 910 nm. An 833 nm LBIC map is shown in Figure 1(a) illustrating regions of high (light gray) and low (dark gray) minority carrier diffusion length. It is evident from Figure 1(a) that there is a wide range of responses of GBs to hydrogen introduced during the annealing of the SiN<sub>x</sub> coating (firing). Some GBs showing strong recombination activity in bare regions are nearly completely passivated (i.e., contrast between GB and surrounding grain is close to zero). Other GBs show almost no response to hydrogen, exhibiting similarly high LBIC contrasts in both bare and SiN<sub>x</sub>-coated regions.

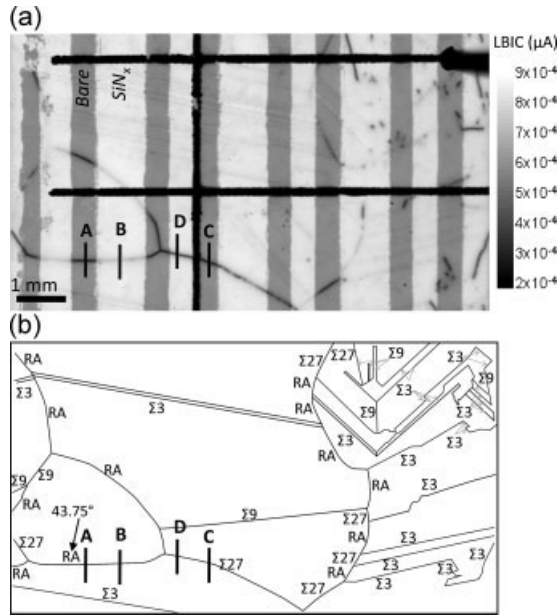


**Figure 1.** LBIC and EBSD of sample. (a) LBIC measurements (833 nm wavelength, 10 μm step size) were used to identify grain boundaries of high and low recombination activity. Dark gray stripes correspond to bare regions, while lighter gray stripes are SiN<sub>x</sub>-coated. Black lines correspond to metallization. (b) Grain boundary types were identified by electron backscatter diffraction. Labels A to D correspond to the regions of interest. Grain boundaries labeled RA refer to CSL higher than 181 but well-known misorientation angles as shown in regions A and B.

The same area was also mapped using electron backscatter diffraction (EBSD) to determine the crystallographic orientations of the GBs under study. Previous works have shown a strong interdependence between GB recombination activity, GB type [10,11], and the density of metal silicide precipitates [12]. When possible, the GB was classified by its coincidence site lattice (CSL) index ( $\Sigma$  value); otherwise when the  $\Sigma$  value exceeds 181, the GB is denoted as “random angle” (RA). This notation does not imply the angles cannot be determined; on the contrary, it usually corresponds to well-established high-angle misorientations.

Guided by the LBIC map of Figure 1, four regions (labeled A, B, C, D in Figure 1) were selected for closer analysis. The regions were selected from two different types of GBs: an RA GB, which corresponds to a misorientation of 43.8° that passivated due to hydrogenation, and a  $\Sigma$ 27a GB, 31.2° misorientation that did not exhibit an electrical improvement after passivation. From each GB, one bare region and one SiN<sub>x</sub>-coated region were selected. High-resolution LBIC linescans at 833 and 910 nm were taken; these are shown in Figure 2, where the sub-figures (a–d) correspond to the labels (A–D) in Figure 1.

The high-resolution LBIC linescans (Figure 2) were fit to a model [13], which considers the GB as a two-dimensional interface between neighboring grains of uniform diffusion length; the model outputs the effective surface recombination velocity (SRV) of the GB. As reported by Micard *et al.* [13], the fitting procedure uses the LBIC value of the plateau level away from the boundary. The SRVs are then obtained by fitting the profiles normalized by the plateau levels to a theoretical

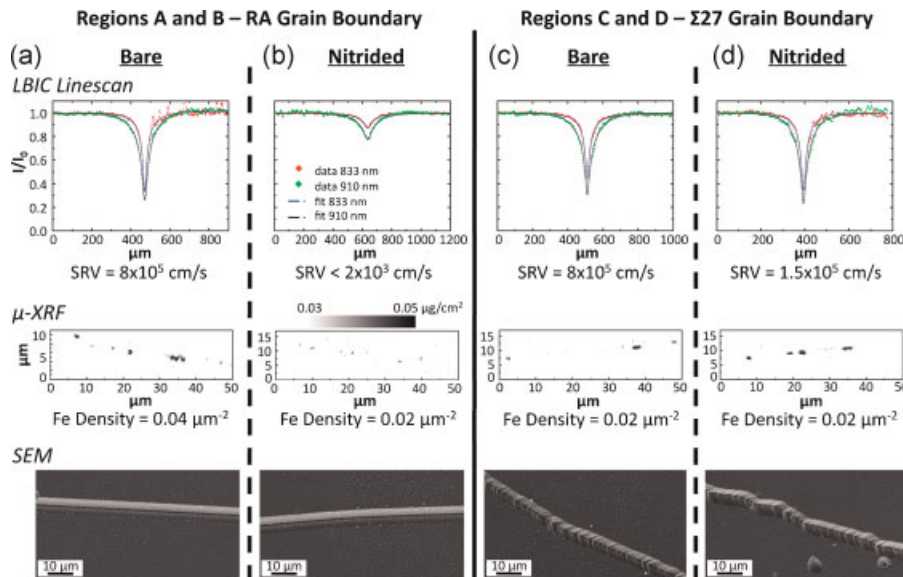


**Figure 2.** Comparison of passivating and non-passivating grain boundaries. Four regions of the sample (a), (b), (c) and (d) corresponding to points A, B, C, and D from Figure 1 were studied by high-resolution LBIC,  $\mu$ -XRF, and SEM.  $\mu$ -XRF data shows Fe-rich particles, given in a real density (particles/ $\mu$ m<sup>2</sup>) along the GB, accurate to within an order of magnitude based on the calculated exit angle of the grain boundary. SEM images show a significant difference in the order and spacing of dislocation etch pits along the two different boundaries. This figure is available in color online at [www.interscience.wiley.com/journal/PIP](http://www.interscience.wiley.com/journal/PIP)

expression. The calculated SRVs are only slightly dependent on injection level; the uncertainties due to differences in injection levels between the nitride-coated and bare regions is estimated to be less than 20%.

The SRV in both the RA and  $\Sigma 27$  GBs was  $8 \times 10^5$  cm/s in the bare regions. In the  $\text{SiN}_x$ -coated regions, this RA GB was observed to have a marked decrease in LBIC contrast, corresponding to a reduction of the SRV to below  $2 \times 10^3$  cm/s. Conversely, this  $\Sigma 27$  GB showed a mild reduction in LBIC contrast, corresponding to an SRV of  $1.5 \times 10^5$  cm/s.

Of interest is the fact that the LBIC linescan profile of the nitrated boundary in Figure 2(d) has a larger contrast than the bare boundary in Figure 2(c), even though the estimated SRV is lower. This apparent discrepancy can be explained by differences in bulk minority carrier diffusion length. The bulk minority carrier diffusion length in the nitride-coated region ( $L_{\text{diff}} = 200\text{--}300 \mu\text{m}$ ) is larger than in the bare regions ( $L_{\text{diff}} = 130 \mu\text{m}$ ), thus a smaller SRV in  $\text{SiN}_x$ -coated region can produce a larger LBIC contrast.

Synchrotron-based X-ray fluorescence microscopy ( $\mu$ -XRF, Figure 2) was used to detect metal silicide nanoprecipitates at these GBs. At Beamline 2-ID-D [14] at the Advanced Photon Source of Argonne National Laboratory, a beam of 10 keV X-rays focused to a 200 nm beam-spot size was used to map the four regions of interest. These maps revealed the presence of Fe-rich particles between 50 nm and 2  $\mu\text{m}$  in diameter decorating the GBs. It should be noted that an incoming X-ray energy of 10 keV permits the detection by  $\mu$ -XRF of the most common and detrimental metallic species in silicon (i.e., Cu, Ni, Fe, Cr); however, only iron was found during these scans. The angle of the GB relative to the sample surface was estimated from the elastically scattered X-ray signal, and the approximate density of the precipitates decorating the grain was calculated. These  $\mu$ -XRF results confirm the presence of Fe in the sample, which is known to be a major source of recombination activity in mc-Si solar cells [15]. Previous reports have shown that the composition of these particles along GBs is mostly  $\text{FeSi}_2$  [16]. Despite the fact that GB SRV was found to vary over two orders of magnitude (Figure 2), the density of Fe particles was found to be similar along these two GBs investigated, suggesting that the post-passivation recombination activity of the GB shown in Figure 2(d) cannot be singularly attributed to the presence of the detected Fe-rich nanoprecipitates at these spatial densities.

Finally, to reveal dislocations present along the GBs, the sample was defect etched. After removal of the metallization and  $\text{SiN}_x$  layer by etching in HF, one side of the sample was polished, and then cleaned in a 9:1 by volume solution of nitric:hydrofluoric acids for 30 s. Next, the sample was etched in a Sopori mix [17] while agitated for 30 s and finally rinsed in deionized water and air-dried. This process revealed  $\sim 5 \mu\text{m}$  etch pits where dislocations exit the surface of the sample.

Scanning electron microscope (SEM) images of the four regions of interest along the RA and  $\Sigma 27$  GBs are shown in

Figure 2. The absence of individual observable etch pits along the RA GB indicates a high degree of order; the dislocation cores of the misfit dislocations present along the boundary are so close together that etch pit counting is not possible. This is consistent with literature reports of misfit dislocation spacing on the order of a couple to tens of nanometers, depending on the angle of misorientation between adjacent grains [18].

On the other hand, the  $\Sigma 27$  GB appears jagged (faceted) with a quantifiable number of etch pits. The spacing between the etch pits in this  $\Sigma 27$  boundary varies from 0.5 to 2  $\mu\text{m}$ , which is two orders of magnitude higher than the typical distance between regularly spaced misfit dislocations [19]. These dislocations are positioned at the corners of step-like features with a consistent angle of  $160^\circ$ . The origin of these etch pits is most likely related to the GB faceting, as described by Andreeva *et al.* [19], where  $\Sigma 27$  boundaries were found to be structurally unstable with a tendency to facet along the  $\{111\}$  planes of the adjacent grains. Higher-order twin boundaries ( $\Sigma 3^n$ ) are known to facet, often after heat treatments [20]. The facets are usually well defined with respect to the CSL GB and are normally parallel to close-packed planes of the CSL GB. TEM investigations have demonstrated the instability of  $\Sigma 27$  boundaries in silicon, which tend to dissociate into a series of 100 nm triangular grains, consisting of a coherent  $\Sigma 3$ , a  $\{122\}$   $\Sigma 9$ , and a  $\{111\}/\{115\}$   $\Sigma 9$  boundary, which is consistent with the  $160^\circ$  angle we report [21]. Note that faceting has also been reported to increase  $\Sigma 27$  GB recombination activity; electron-beam-induced current measurements have shown that the SRV for the symmetric orientation of the  $\Sigma 27$  GB is an order of magnitude smaller than the corresponding asymmetric (faceted) orientations of the GB [19–22].

Figure 3 compares the LBIC contrast before and after passivation for all the GBs that were long enough to have a region in the bare and  $\text{SiN}_x$ -coated stripes. LBIC contrast of a given GBs is defined by

$$C = \frac{I_{\text{grain}} - I_{\text{GB}}}{I_{\text{grain}}}, \quad (1)$$

where LBIC intensity ( $I$ ) was measured at the GB and within the grain (data shown in Figure 1(a)), providing a quantitative measure of the recombination activity of the GB.

Figure 3 illustrates the effectiveness of hydrogen passivation as a function of GB character. The recombination activity (LBIC contrast) of the same GBs is evaluated with and without a passivating  $\text{SiN}_x$  coating. Data points falling well below the 1:1 line represent GBs that passivated well.

From Figure 3, two classes of GBs can be distinguished, typified by GBs (A,B) and (C,D). GBs with LBIC contrast that reduces significantly after passivation exhibit negligible faceting, and no discernable dislocation etch pits. Meanwhile, GBs with unchanged or even higher LBIC contrast after passivation possess a disordered/faceted characteristic (see SEM images in Figure 3). For these

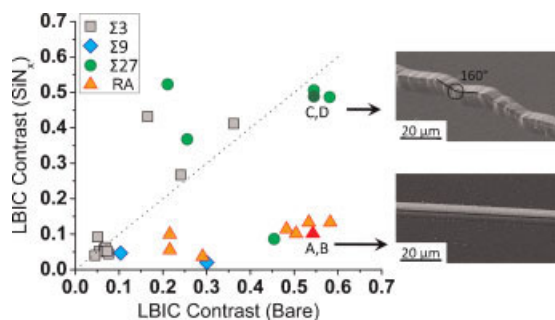


**Figure 3.** LBIC contrast of long grain boundaries. LBIC contrast before and after passivation is compared for individual GBs. The dotted diagonal line represents zero passivation improvement. Data points falling well below this line correspond to grain boundaries that are effectively passivated. Conversely, GBs falling nearby this line do not passivate. Scanning electron micrographs of typical passivating and non-passivating grain boundaries are illustrated to the right; labels A, B, C, and D refer to regions designated in Figures 1 and 2. Note the  $160^\circ$  faceting angle characteristic of non-passivating GBs. This figure is available in color online at [www.interscience.wiley.com/journal/PIP](http://www.interscience.wiley.com/journal/PIP)

GBs, we compare LBIC contrast versus the density of visible etch pits per unit length along the GB (Figure 4). The correlations between etch pit density and LBIC contrast before and after hydrogenation (Figure 4) present a clear trend of higher passivation efficacy with lower dislocation etch pit density. This observation is in line with work by Donolato, who related electron beam induced current (EBIC) to the density of dislocations in a boundary plane [23].

The dependence of LBIC contrast on etch pit density (Figure 4) suggests that dislocations, possibly related to faceting, along the GB are the primary defect limiting improvement of GB recombination activity after hydrogen passivation. Due to the presence of large Fe-silicide precipitates detected along the GBs (Figure 2), one could also expect impurity point defects or smaller precipitates (below our  $\mu$ -XRF detection limit) to decorate the dislocations, contributing to their recombination activity. This would be consistent with previous work suggesting that the interaction between Fe and GB structure governs the recombination activity of certain GBs [12,24–26]. Our observations are also consistent with a recent report by Sarau *et al.* [27], which indicates that the stress associated with this type of GB faceting is correlated to GB electrical activity.

In conclusion, LBIC studies on a specially prepared mc-Si solar cell sample containing mm-wide stripes of bare and  $\text{SiN}_x$ -coated regions indicate that the recombination activity at some GBs reduces significantly upon hydrogen passivation, whereas other GBs do not, consistent with literature reports. Our detailed analytical investigations demonstrate that defect microstructure plays a dominant role in determining passivation efficacy.  $\mu$ -XRF, EBSD, and defect etching reveal that the density of countable etch pits, likely related to the high degree of faceting of the GB,

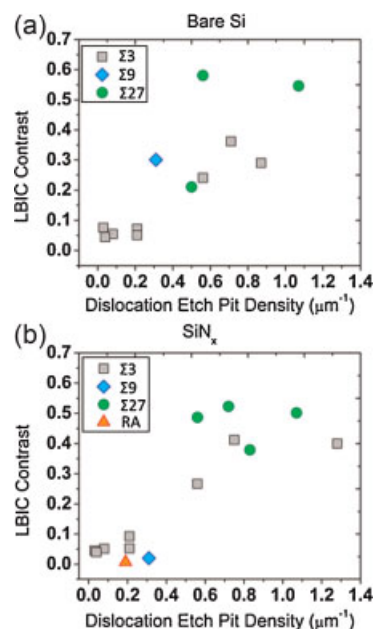


**Figure 4.** Recombination activity of grain boundaries by type and dislocation density for (a) bare silicon and (b) hydrogen passivated regions. LBIC contrast is plotted versus dislocation etch pit density (EPD) for GBs exhibiting little to no improvement after hydrogenation (upper points in Figure 3). Note a strong proportional dependence of GB recombination activity on EPD both before and after hydrogenation. This figure is available in color online at [www.interscience.wiley.com/journal/PIP](http://www.interscience.wiley.com/journal/PIP)

are the principal defect indicating post-passivation GB recombination activity. In comparison, Fe-rich precipitate decoration was found to play a less significant role. These results point to the importance of efforts to control GB microstructure, including GB type and dislocation density, during the growth and processing of mc-Si solar cells.

## ACKNOWLEDGEMENTS

S. Bernardis, K. Hartman and Y.S. Lee are acknowledged for experimental assistance. Support for this research was provided by the U.S. Department of Energy, under contract number DE-FG36-09GO19001, and through the generous support of Doug and Barbara Spreng and the Chesonis Family Foundation. S. Hudelson and D.P. Fenning acknowledge the support of the National Science Foundation, and B.K. Newman support of the Clare Boothe Luce Foundation. Use of the Advanced Photon Source at Argonne National Laboratory was supported by the U.S. Department of Energy, Office of Science, Office of Basic Energy Sciences, under contract number DE-AC02-06CH11357.

## REFERENCES

1. Martinuzzi S, Périchaud I, Warchol F. Hydrogen passivation of defects in multicrystalline silicon solar

- cells. *Solar Energy Materials and Solar Cells* 2003; **80**: 343–353.
- Hanoka JI, Seager CH, Sharp DJ, Panitz JKG. Hydrogen passivation of defects in silicon ribbon grown by the edge-defined film-fed growth process. *Applied Physics Letters* 1983; **42**: 618–620.
  - Geiger P, Kragler G, Hahn G, Fath P. Influence of hydrogen passivation on majority and minority charge carrier mobilities in ribbon silicon. *Solar Energy Materials and Solar Cells* 2005; **85**: 559–572.
  - Chen J, Yang D, Xi Z, Sekiguchi T. Electron-beam-induced current study of hydrogen passivation on grain boundaries in multicrystalline silicon: influence of GB character and impurity contamination. *Physica B: Condensed Matter* 2005; **364**: 162–169.
  - Rinio M, Kaes M, Hahn G, Borchert D. Hydrogen passivation of extended defects in multicrystalline silicon solar cells. *Proceedings of the 21st EUPVSEC*, Dresden, Germany, 2006.
  - Zuschlag A, Micard G, Junge J, Käs M, Seren S, Hahn G, Coletti G, Jia G, Seifert W. Extraction of the surface recombination velocity and diffusion length from LBIC and EBIC measurements at grain boundaries in mc silicon. *Proceedings of the 23rd IEEE Photovoltaic Specialists Conference*, San Diego, USA, 2008.
  - Junge J, Herguth A, Seren S, Hahn G. Reducing the impact of metal impurities in block-cast mc silicon. *Proceedings of the 24th EUPVSEC*, Hamburg, Germany, 2009.
  - Geerligs LJ, Komatsu Y, Röver I, Wambach K, Yamaga I, Saitoh T. Precipitates and hydrogen passivation at crystal defects in n- and p-type multicrystalline silicon. *Journal of Applied Physics* 2007, **102**, 093702.
  - Isenberg J, Bartels O, Warta W. Separation of bulk diffusion length and rear surface recombination velocity in SR-LBIC mappings. *Proceedings of the 29th IEEE Photovoltaic Specialists Conference*, 2002, 328–331.
  - Chen J, Sekiguchi T, Yang D. Electron-beam-induced current study of grain boundaries in multicrystalline Si. *Physica Status Solidi C* 2007; **4**: 2908–2917.
  - Chen J, Sekiguchi T, Yang D, Yin F, Kido K, Tsurukawa S. Electron-beam-induced current study of grain boundaries in multicrystalline silicon. *Journal of Applied Physics* 2004; **96**: 5490.
  - Buonassisi T, Istratov AA, Pickett MD, Marcus MA, Ciszek TF, Weber ER. Metal precipitation at grain boundaries in silicon: dependence on grain boundary character and dislocation decoration. *Applied Physics Letters* 2006; **89**: 042102.
  - Micard G, Seren S, Hahn G. Quantitative interpretation of light beam induced current contrast profiles: evaluating the influence of a near grain boundary. *Proceedings of the 24th EUPVSEC*, Hamburg, Germany, 2009.
  - Cai Z, Lai B, Yun W, McNulty I, Khounsary A, Maser J, Ilinski P, Legnini D, Trakhtenberg E, Xu S, Tieman B, Wiemerslage G, Gluskin E. Performance of a high-resolution X-ray microprobe at the Advanced Photon Source. *Synchrotron Radiation Instrumentation: SR 199: Eleventh US National Conference*, 2000, 31–34.
  - Coletti G, Kvande R, Mihailetschi VD, Geerligs LJ, Arnberg L, Ovrelid EJ. Effect of iron in silicon feedstock on p- and n-type multicrystalline silicon solar cells. *Journal of Applied Physics* 2008; **104**: 104913-11.
  - Buonassisi T, Istratov AA, Heuer M, Marcus MA, Jonczyk R, Isenberg J, Lai B, Cai ZH, Heald S, Warta W, Schindler R, Willeke G, Weber ER. Synchrotron-based investigations of the nature and impact of iron contamination in multicrystalline silicon solar cells. *Journal of Applied Physics* 2005; **97**: 074901.
  - Sopori BL. A new defect etch for polycrystalline silicon. *Journal of the Electrochemical Society* 1984; **131**: 667.
  - Babcock SE, Balluffi RW. Secondary grain-boundary dislocation-structures in gold and silver (001) twist boundaries revisited. *Philosophical Magazine A* 1987; **55**(5): 643.
  - Andreeva AV, Bazhenov AV, Bulenkov NA, Firso AA. Structural and photoelectrical properties of a third-order twin boundary ( $\Sigma = 27$ ) in silicon. *Physica Status Solidi A* 1988; **106**: 351.
  - Sukhomlin G, Andreeva A. Particular properties of  $\Sigma = 3^{\text{rd}}$  boundaries in F.C.C. polycrystals. *Physica Status Solidi A* 1983; **78**: 333.
  - Garg A, Clark WAT, Hirth JP. Dissociated and faceted large-angle coincident-site-lattice boundaries in silicon. *Philosophical Magazine A* 1989; **59**(3): 479–499.
  - Chen B, Chen J, Sekiguchi T, Saito M, Kimoto K. Structural characterization and iron detection at  $\Sigma 3$  grain boundaries in multicrystalline silicon. *Journal of Applied Physics* 2009; **105**: 113502–113505.
  - Donolato C. The relation between EBIC contrast and recombination velocity of a grain boundary. *Materials Science and Engineering* 1994; **B24**: 61–63.
  - Sopori BL, Deng X, Benner JP, Rohatgi A, Sana P, Estreicher SK, Park YK, Roberson MA. Hydrogen in silicon: a discussion of diffusion and passivation mechanisms. *Solar Energy Materials and Solar Cells* 1996; **41**: 159–169.
  - Seifert W, Morgenstern G, Kittler M. Influence of dislocation density on recombination at grain boundaries in multicrystalline silicon. *Semiconductor Science and Technology* 1993; **8**: 1687–1691.
  - Kutsukake K, Usami N, Fujiwara K, Nose Y, Nakajima K. Influence of structural imperfection of  $\Sigma 5$  grain boundaries in bulk multicrystalline Si on their electrical activities. *Journal of Applied Physics* 2007; **101**: 063509-5.
  - Sarau G, Becker M, Christiansen S, Holla M, Seifert W. Micro-Raman mapping of residual stresses at grain boundaries in multicrystalline block cast silicon solar cell material: their relation to the grain boundary microstructure and recombination activity, *Proceedings of the 24th EUPVSEC*, Hamburg, Germany, 2009.